Journal of Applied Physics

PLEASE CITE THIS ARTICLE AS DOI: 10.1063/5.0004552

All-optical nanophotonic resonant element for switching and routing applications exploiting graphene saturable absorption

Thomas Christopoulos,[1, a)] Vasileios G. Ataloglou,[2] and Emmanouil E. Kriezis[1]
[1)] *School of Electrical and Computer Engineering, Aristotle University of Thessaloniki (AUTH), Thessaloniki 54124, Greece*
[2)] *Department of Electrical and Computer Engineering, University of Toronto, M5S 3G4 Toronto, ON, Canada*

(Dated: 25 May 2020)

A silicon disk resonator overlaid with a uniform graphene layer in an add-drop configuration is proposed as an all-optical routing element. Operation is based on the saturable absorption effect provided by the graphene layer. The element is thoroughly analyzed as a two-channel device, in the context of an appropriate nonlinear framework combining perturbation theory and temporal coupled-mode theory. Taking into consideration the primary nonlinear effect which is graphene saturable absorption, a design path is carefully developed that eventually leads to a traveling-wave resonant element with low power requirements, low insertion loss, high extinction ratio and sufficient bandwidth. In a subsequent step, other important nonlinear effects originating from graphene and the silicon disk, including the Kerr effect and free carrier effects, are considered and means for counterbalancing their action are demonstrated. Low control power of 9 mW together with a bandwidth of 20 GHz are shown possible, with insertion loss of almost 3 dB and extinction ratio over 10 dB in both ports (add and drop).

I. INTRODUCTION

For the past decade, graphene has attracted the increased attention of the scientific community, mostly because of its unique thermal, mechanical, electrical, and optical properties.[1] Optical response is broadband, spanning from the far- to the near-infrared (NIR) frequency regimes, and it is associated to the surface conductivity which additionally demonstrates extensive levels of tunability. This allows for diverse photonic applications,[2,3] with the most researched topics being graphene-enhanced waveguides[4] and resonators,[5] mostly for electro-absorption modulation.[6–9] Recent measurements confirmed that graphene additionally exhibits a strongly nonlinear optical response which is commonly translated into third-order ($\chi^{(3)}$-type) optical phenomena (Kerr effect, two-photon absorption),[10,11] being themselves vastly tunable.[12] Since this ascertainment arose, various all-optical switching elements based on graphene have been reported in the literature.[13–17]

Another notable graphene property is the nonlinear quench of its linear losses, a phenomenon that is well known in semiconductors as saturable absorption (SA).[18] The origins of SA in graphene[19] are the same as those in semiconductors, but the phenomenon establishes for appreciably lower light illumination intensities.[20,21] In fact, saturable absorption was the first nonlinear effect of graphene that was demonstrated and successfully exploited in various fiber lasers, back in 2010 and shortly afterwards.[22–24] Later, graphene SA was utilized in other photonic circuits,[25–27] mostly due to the maturity of the chemical vapor deposition (CVD) technique that allows its growth. Subsequent experimental works were published,[18] and the loss saturation effect originating from graphene was measured in various waveguide structures of wire[26,28–30] or slot-type,[31] in silicon-on-insulator (SOI) and silicon-nitride platforms, and recently in a plasmonic waveguide.[32] The path of increased complexity that experimental works follow, starting from the simpler fiber-based applications and gradually turning to more demanding on-chip realizations, reflects the growing challenges of each utilization.

The idea of loss manipulation can be further enhanced when resonant cavities are involved, mainly for two reasons. On one side, cavities provide the means to enhance the light-graphene interaction by the consequent intensity build-up provided under resonance conditions. On the other side, they also intensify the loss manipulation effect, owing to the presence of a critical coupling condition, which allows the transition from a low to high transmission state only with a minor change in light absorption. Favorably, this approach is further backed by the recent development of a strict and accurate mathematical framework which allows for the efficient computational analysis of cavity systems exhibiting SA,[33,34] without resorting to cumbersome full-wave nonlinear simulations. Naturally, incorporating graphene in a resonant structure to advantageously exploit saturable absorption is the next challenging step. A computational verification that such a system, being as close as possible to a practical one, has reasonable performance metrics is an essential step.

Capitalizing on the ideas briefly introduced above and motivated by the everlasting demand for faster and more power-efficient integrated components, and targeting on bridging the gap between innovative physical phenomena and their exploitation for real-world applications, we propose, analyze and design a graphene-enhanced silicon disk resonator in an add-drop configuration, appro-

---

[a)] Electronic mail: cthomasa@ece.auth.gr

priate for all-optical routing applications. Add-drop filters are four-port, frequency-selective photonic devices, commonly used for multiplexing/routing in wavelength-division multiplexing (WDM) systems, but their unique response can be exploited in other applications, as well. The mathematical framework earlier mentioned permits the in-depth and comprehensive study of the proposed resonant device and elegantly leads to the extraction of simple design rules that govern its operation. Importantly, it allows to simultaneously take into account all relevant multi-channel linear and nonlinear effects involved (saturable absorption, Kerr effect, linear ohmic and radiation losses); an approach that is not in any case trivial. Thus, it consists a powerful tool for the analysis and design of complex nonlinear structures, which furthermore employ 2D materials. The routing operation is all-optically controlled by a different guided signal, which carries adequate power to suppress graphene losses and render the resonant cavity in critical coupling conditions. Such two-channel operation, although intuitively expected, only recently has started to get explored in the literature.[35] Ultimately, the proposed nonlinear traveling-wave (TW) cavity is prudently designed to exhibit satisfactory performance in both ports, namely low insertion losses, high extinction ratios, and high bandwidth, bringing all-optical designs a step closer to practical realization and narrowing the gap with the more mature electro-optical platforms.

The rest of the paper is organized as follows. In Sec. II the loss saturation mechanism of graphene is presented and incorporated into a mathematical framework that combines first-order perturbation theory with temporal coupled-mode theory (CMT), which is capable of describing nonlinear resonant cavities. Other nonlinear interactions, such as the Kerr effect, are also allowed by the framework and are indeed included. Sec. III is devoted to the design strategy, focusing on a resonant cavity cast in an add-drop configuration with two parallel feeding waveguides. For the coupled cavity to act as a routing element with high performance metrics, a specific design approach under appropriate simplifying assumptions is outlined, leading to closed-form expressions. Next, in Sec. IV, a practical graphene-enhanced silicon disk TW resonator, acting as an SA-driven all-optical routing element, is assessed. Its performance metrics are thoroughly extracted and its dynamic response is carefully evaluated. Finally, our work concludes with Sec. V.

II. THEORETICAL FRAMEWORK

In this section we briefly present an appropriate framework combining perturbation theory and temporal coupled-mode theory, capable of handling the nonlinear response of resonant structures excited by two channels (wavelengths). Through the perturbation theory method, the nonlinear effects associated with sheet and bulk materials are quantified in terms of complex shifts in resonance frequencies. Then, CMT is utilized to analyze the response of a nonlinear graphene-comprising resonator, side-coupled to two access waveguides.

A. Perturbation theory for graphene saturable absorption

The electromagnetic properties of graphene can be modeled through the induced linear and nonlinear surface current densities. The linear surface current density is given as $\mathbf{J}_s = \sigma_1 \mathbf{E}_\parallel$, where $\mathbf{E}_\parallel$ is the tangential to the graphene sheet electric field and σ_1 is the total linear conductivity, encompassing two distinct mechanisms of single-photon absorption, namely the intraband and interband absorption.[36–38] Both absorption mechanisms saturate under a relatively strong electric field, giving rise to an effect known as saturable absorption. The origins of SA lie in the electron accumulation in the conduction band under light illumination with high intensity and the Pauli exclusion principle, preventing the excitation of additional electrons.[18,19,35,39] For a Fermi level below half the illuminating photon energy $|\mu_c| < \hbar\omega/2$, the interband absorption dominates over the intraband term, while it saturates for a considerably lower level of the applied electric field intensity.[19] Therefore, the intraband term can be regarded as intensity-independent and the overall linear conductivity of graphene takes the form (for an $\exp\{+j\omega t\}$ time-harmonic convention)[19,40]

$$\sigma_1 = \sigma_{\text{intra,Re}} + j\sigma_{\text{intra,Im}} + \sigma_{\text{inter,Re}}(\mathbf{E}_\parallel) + j\sigma_{\text{inter,Im}}(\mathbf{E}_\parallel), \tag{1}$$

where

$$\sigma_{\text{inter,Re}}(\mathbf{E}_\parallel) = \frac{\sigma_{\text{inter}}^{(0)}}{\sqrt{1 + 3|\mathbf{E}_\parallel|^2/E_{\text{sat}}^2}}, \tag{2a}$$

$$\sigma_{\text{inter,Im}}(\mathbf{E}_\parallel) = \sigma_{\text{inter}}^{(0)} \frac{1 - \exp\{-\eta_1 \sqrt{|\mathbf{E}_\parallel|^2/E_{\text{sat}}^2}\}}{\sqrt{1 + \left(\eta_1^2 |\mathbf{E}_\parallel|^2/E_{\text{sat}}^2\right)^{0.4}}}, \tag{2b}$$

with $\sigma_{\text{intra}} = \sigma_{\text{intra,Re}} + j\sigma_{\text{intra,Im}} = 0.3 - j3.4\ \mu\text{S}$ and $\sigma_{\text{inter}}^{(0)} = 60.9\ \mu\text{S}$,[36,37] referring to the intraband and interband conductivity, respectively, for a Fermi level $\mu_c = 0$ at 1550 nm; $E_{\text{sat}} = 27.5$ kV/cm is the equivalent electric field saturation level (corresponding to[20,21] $I_{\text{sat}} = E_{\text{sat}}^2/2\eta_0 = 1\ \text{MW/cm}^2$) and $\eta_1 = (46.2\ \text{rad/ps})/\omega$ is a dimensionless coefficient,[40] inversely proportional to the operating frequency ω. Note that SA affects both the real and the imaginary parts of the interband conductivity of graphene, while the intraband terms are considered constant as they saturate at much higher field intensities. The dependance of Eqs. (2) on the applied field intensity is depicted in Fig. 1, revealing the saturation behaviour in both real and imaginary parts of graphene interband conductivity. We must note that the form of Eqs. (1) and (2) differs from the conventional $1/(1 + I/I_{\text{sat}})$ model, well describing a two-level system and solely referring to linear loss saturation. The model adopted here exclusively

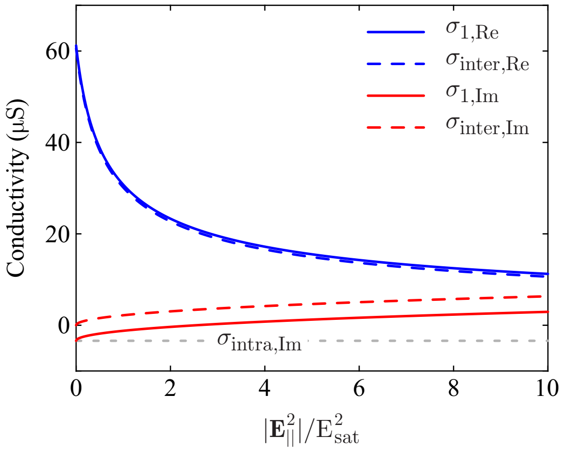

FIG. 1. Graphene conductivity saturation with respect to the applied electric field intensity at the wavelength of 1550 nm for $\mu_c = 0$. Its real part, representing ohmic loss, strongly saturates while its imaginary part (dielectric properties of graphene) changes sign.

refers to graphene SA and, importantly, takes into account the saturation in the imaginary part of σ_1 (dielectric properties of graphene).

The overall effect of graphene on the resonance characteristics of the cavity is relatively weak, thus perturbation theory can be utilized to determine the response of the resonant system.[41] Given that both interband and intraband conductivity contributions are considered as perturbations, the following equation stands,[34]

$$\Delta\omega_{(k)} = \frac{j \iint_S \mathbf{J}_{s,(k)} \cdot \mathbf{E}^*_{\parallel,(k)} \mathrm{d}S}{\iiint_V \varepsilon_0 \frac{\partial\{\omega\varepsilon_r\}}{\partial\omega} |\mathbf{E}_{(k)}|^2 \mathrm{d}V + \iiint_V \mu_0 |\mathbf{H}_{(k)}|^2 \mathrm{d}V}, \tag{3}$$

where the integration in the numerator is exclusively performed on graphene, justifying the reduction by one order in domain dimensions. We must note, as well, that the linear properties of graphene are exclusively introduced through the numerator of Eq. (3), determining how graphene affects the cavity characteristics after its incorporation. Given that the interband conductivity term saturates, this phenomenon is inherited to the respective perturbation theory term. The adopted approach considering graphene in its entirety as the cavity perturbation, results in the absence of its contribution in the unperturbed system [denominator of Eq. (3)].[42] Nevertheless, this does not introduce any remarkable error, since its contribution is rather weak at the NIR frequency range under study. Finally, we have allowed for two-wave operation by introducing the variable $k = \{c, p\}$, referring either to the strong control or to the weak probe wave.

By replacing the current density $\mathbf{J}_{s,(k)}$ in Eq. (3) using Ohm's law and the model of the surface conductivity introduced in Eq. (1), we can calculate the graphene-induced frequency shift and the cavity photon lifetime corresponding to graphene loss. To simplify the resulting formulae, it is assumed that the control signal is much stronger compared to the probe, $\mathbf{E}_{(c)} \gg \mathbf{E}_{(p)}$. Therefore, the surface conductivity in Eq. (1) solely saturates due to the control signal. Then, the following expressions are derived for the power-independent intraband terms

$$\Delta\omega_{\mathrm{intra},(k)} = \frac{-\iint_S \sigma_{\mathrm{intra,Im}} |\mathbf{E}_{\parallel,(k)}|^2 \mathrm{d}S}{\iiint_V \varepsilon_0\varepsilon_r |\mathbf{E}_{(k)}|^2 \mathrm{d}V + \iiint_V \mu_0 |\mathbf{H}_{(k)}|^2 \mathrm{d}V}, \tag{4a}$$

$$\frac{1}{\tau_{\mathrm{intra},(k)}} = \frac{\iint_S \sigma_{\mathrm{intra,Re}} |\mathbf{E}_{\parallel,(k)}|^2 \mathrm{d}S}{\iiint_V \varepsilon_0\varepsilon_r |\mathbf{E}_{(k)}|^2 \mathrm{d}V + \iiint_V \mu_0 |\mathbf{H}_{(k)}|^2 \mathrm{d}V}, \tag{4b}$$

and the power-dependent interband terms

$$\Delta\omega_{\mathrm{SA},(k)} = \frac{-\iint_S \sigma_{\mathrm{inter,Im}}(\mathbf{E}_{\parallel,(c)}) |\mathbf{E}_{\parallel,(k)}|^2 \mathrm{d}S}{\iiint_V \varepsilon_0\varepsilon_r |\mathbf{E}_{(k)}|^2 \mathrm{d}V + \iiint_V \mu_0 |\mathbf{H}_{(k)}|^2 \mathrm{d}V}, \tag{5a}$$

$$\frac{1}{\tau_{\mathrm{SA},(k)}} = \frac{\iint_S \sigma_{\mathrm{inter,Re}}(\mathbf{E}_{\parallel,(c)}) |\mathbf{E}_{\parallel,(k)}|^2 \mathrm{d}S}{\iiint_V \varepsilon_0\varepsilon_r |\mathbf{E}_{(k)}|^2 \mathrm{d}V + \iiint_V \mu_0 |\mathbf{H}_{(k)}|^2 \mathrm{d}V}. \tag{5b}$$

Note that the power-dependent perturbation terms in Eqs. (5) solely involve the strong control signal, reflecting the fact that SA appears only due to this wave; the terminology cross-SA might then be used, echoing that the loss saturation experienced by the probe signal is due to the strong control wave.[35] Besides, the above equations are written in such a general form, so that any model of saturation can be introduced, either that of Eqs. (2) or any other that presumably will emerge in the literature. For the followed interpretation, bulk material dispersion in ε_r has been neglected, typically being mild for most photonic materials in the NIR. Thus, the stored energy is calculated simply as $W_{(k)} = (1/4)\iiint_V \varepsilon_0\varepsilon_r|\mathbf{E}_{(k)}|^2\mathrm{d}V + (1/4)\iiint_V \mu_0|\mathbf{H}_{(k)}|^2\mathrm{d}V$. This remark ties well with Eq. (4b), from which the definition of the quality factor, owing to intraband loss mechanism, can be recalled, i.e., $1/\tau_{\mathrm{intra},(k)} = 2P_{\mathrm{loss}}/4W_{(k)} = \omega_{(k)}/2Q_{\mathrm{intra},(k)}$,[43] with $\omega_{(k)}$ being the respective resonance frequency. Finally, it is instructive to mention that for graphene exhibiting a Fermi level of $\mu_c \approx 0$ in the near-infrared regime, the frequency shifts associated with the intraband and the interband mechanisms have different signs, partially canceling each other, as evident from the red and gray curves in Fig. 1.

B. Perturbation theory for other nonlinear effects

In a realistic resonant system, other nonlinear effects are also acting in addition to SA and they should be incorporated; they include the Kerr effect, two-photon absorption (TPA), and free-carrier effects (FCEs), both in bulk materials and in graphene. The perturbation theory approach is to be followed for this purpose, as well, with the above phenomena being well described in the literature of resonant cavities.[15,44–48] Thus, we solely present the emerged resonance frequency shift terms, without resorting to the cumbersome presentation of the respective mathematical analysis, which can be found in the above-cited works.

The Kerr effect induces a resonance frequency shift due to self-phase modulation (SPM) and cross-phase modulation (XPM), since two waves are employed. However, given that the control signal is much stronger compared to the probe signal, out of the four possible contributions only two are found important; the SPM of the control wave ($\Delta\omega_{\mathrm{SPM},(c)}$) and the XPM experienced by the probe wave due to the presence of the control wave ($\Delta\omega_{\mathrm{XPM},(pc)}$). Both graphene and the underlying bulk materials might contribute to the Kerr nonlinearity and are thus introduced in the calculation through separate contributions,[48] i.e.,

$$\Delta\omega_{\mathrm{SPM},(c)} = -\frac{\dfrac{1}{3}\varepsilon_0^2\omega_{(c)}c_0 \iiint_V n_2 n_0^2\,\mathcal{U}_{\mathrm{SPM}}(\mathbf{E}_{(c)})\mathrm{d}V + \dfrac{1}{4}\iint_S \sigma_{3,\mathrm{Im}}\,\mathcal{U}_{\mathrm{SPM}}(\mathbf{E}_{\parallel,(c)})\mathrm{d}S}{\iiint_V \varepsilon_0\varepsilon_r|\mathbf{E}_{(c)}|^2\mathrm{d}V + \iiint_V \mu_0|\mathbf{H}_{(c)}|^2\mathrm{d}V}, \tag{6a}$$

$$\Delta\omega_{\mathrm{XPM},(pc)} = -\frac{\dfrac{2}{3}\varepsilon_0^2\omega_{(c)}c_0 \iiint_V n_2 n_0^2\,\mathcal{U}_{\mathrm{XPM}}(\mathbf{E}_{(p)},\mathbf{E}_{(c)})\mathrm{d}V + \dfrac{1}{2}\iint_S \sigma_{3,\mathrm{Im}}\,\mathcal{U}_{\mathrm{XPM}}(\mathbf{E}_{\parallel,(p)},\mathbf{E}_{\parallel,(c)})\mathrm{d}S}{\iiint_V \varepsilon_0\varepsilon_r|\mathbf{E}_{(p)}|^2\mathrm{d}V + \iiint_V \mu_0|\mathbf{H}_{(p)}|^2\mathrm{d}V}, \tag{6b}$$

where we have defined for brevity the scalar quantities

$$\mathcal{U}_{\mathrm{SPM}}(\mathbf{F}_{(k)}) = 2|\mathbf{F}_{(k)}|^4 + |\mathbf{F}_{(k)}\cdot\mathbf{F}_{(k)}|^2, \tag{7a}$$

$$\mathcal{U}_{\mathrm{XPM}}(\mathbf{F}_{(k)},\mathbf{F}_{(\ell)}) = |\mathbf{F}_{(k)}|^2|\mathbf{F}_{(\ell)}|^2 + |\mathbf{F}_{(k)}\cdot\mathbf{F}_{(\ell)}|^2 + |\mathbf{F}_{(k)}\cdot\mathbf{F}^*_{(\ell)}|^2. \tag{7b}$$

The Kerr effect also induces frequency mixing phenomena that should in principle be taken into account.[49] Nevertheless, if the operating frequencies of the probe and the control waves are well separated, the nonlinear products in the same frequency band, emerging at $2\omega_{(c)}-\omega_{(p)}$ and $2\omega_{(p)}-\omega_{(c)}$, are also well separated and presumably do not lie in the vicinity of a resonance.[45] Additionally, given that only the control wave is strong, the conversion efficiency of such mixing processes will be low.[46,48]

Regarding the two-photon absorption process in graphene, it can be assumed as negligible given that it is unbiased, $\mu_c \approx 0$, in order for the SA effect to dominate.[19] On the other hand, TPA in silicon does exist and could in principle affect the response of the resonant device. Still, having calculated its contribution resorting to a framework already available in the literature,[47] it ends up as being totally unimportant for the power levels that are considered in our work (in the order of few mW). The same is true for free-carrier effects as well, assuming an achievable carrier lifetime in the order of tens of ps. Carrier lifetimes over 100 ps mostly affect the temporal response of the proposed resonant elements due to the carrier recombination process, rather its continuous wave (CW) performance metrics. Finally, we note that the carriers generated in graphene cannot escape in the underlying silicon due to the Schottky barrier formed in the silicon-graphene heterostructure.[50]

C. Coupled-mode theory for two-channel operation in resonators experiencing SA

In this section, the nonlinear terms previously presented are incorporated into the temporal CMT framework, in order to analyze the response of resonant structures consisting of a traveling-wave resonator, side-coupled to two straight access waveguides, as illustrated in Fig. 2. For two-channel operation $\{k,\ell\} = \{p,c\}$, the temporal response is described by the following set of equations:

$$\frac{\mathrm{d}a_{(k)}}{\mathrm{d}t} = j(\omega_{(k)} + \Delta\omega_{\mathrm{intra},(k)} + \Delta\omega_{\mathrm{SA},(k)} + \Delta\omega_{\mathrm{SPM},(k)} + \Delta\omega_{\mathrm{XPM},(k\ell)})a_{(k)}$$

$$-\left(\frac{1}{\tau_{\mathrm{intra},(k)}}+\frac{1}{\tau_{\mathrm{SA},(k)}}+\frac{1}{\tau_{\mathrm{rad},(k)}}+\frac{1}{\tau^{\mathrm{low}}_{e,(k)}}+\frac{1}{\tau^{\mathrm{upp}}_{e,(k)}}\right)a_{(k)}+j\sqrt{\frac{2}{\tau^{\mathrm{low}}_{e,(k)}}}s_{\mathrm{in},(k)}, \tag{8a}$$

$$s_{\mathrm{th},(k)}=s_{\mathrm{in},(k)}+j\sqrt{\frac{2}{\tau^{\mathrm{low}}_{e,(k)}}}a_{(k)}, \tag{8b}$$

$$s_{\mathrm{dr},(k)}=j\sqrt{\frac{2}{\tau^{\mathrm{upp}}_{e,(k)}}}a_{(k)}, \tag{8c}$$

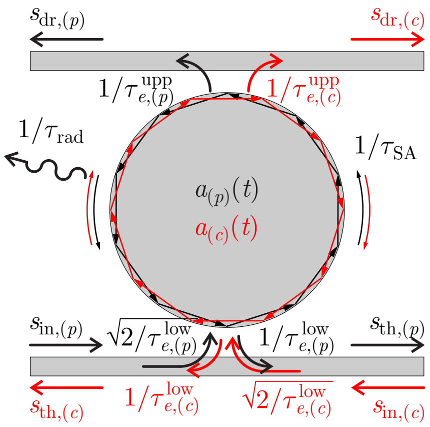
$s_{\mathrm{dr},(p)}$
$s_{\mathrm{dr},(c)}$
$1/\tau^{\mathrm{upp}}_{e,(p)}$
$1/\tau^{\mathrm{upp}}_{e,(c)}$
$1/\tau_{\mathrm{rad}}$
$1/\tau_{\mathrm{SA}}$
$a_{(p)}(t)$
$a_{(c)}(t)$
$s_{\mathrm{in},(p)}$
$\sqrt{2/\tau^{\mathrm{low}}_{e,(p)}}$
$1/\tau^{\mathrm{low}}_{e,(p)}$
$s_{\mathrm{th},(p)}$
$s_{\mathrm{th},(c)}$
$1/\tau^{\mathrm{low}}_{e,(c)}$
$\sqrt{2/\tau^{\mathrm{low}}_{e,(c)}}$
$s_{\mathrm{in},(c)}$

FIG. 2. Schematic of an add-drop filter configuration. Coupling of input waves and loss decay rates are highlighted.

where $a_{(k)}$ is the normalized cavity field amplitude, so that $|a_{(k)}|^2 \equiv W_{(k)}$ expresses the total stored energy in the resonator for each mode and $s_{\mathrm{in/th/dr},(k)}$ stands for the amplitude of the input/output waves, so that $|s_{\mathrm{in/th/dr},(k)}|^2 \equiv P_{\mathrm{in/th/dr},(k)}$ expresses the power flow at the corresponding frequency and port. Several nonlinear frequency shifts are added to the unperturbed resonance frequency $\omega_{(k)}$, in order to capture the effects of the different nonlinear phenomena previously introduced. In addition, the cavity amplitude is decreased by the cavity photon lifetimes associated to the intraband absorption in graphene $\tau_{\mathrm{intra},(k)}$, the interband SA-affected absorption $\tau_{\mathrm{SA},(k)}$, the radiation loss $\tau_{\mathrm{rad},(k)}$, and the coupling loss to the lower and upper waveguides $\tau^{\mathrm{low}}_{e,(k)}$ and $\tau^{\mathrm{upp}}_{e,(k)}$, respectively. Although the two waveguides are allowed to be unevenly coupled to the resonator (in general, $\tau^{\mathrm{low}}_{e,(k)} \neq \tau^{\mathrm{upp}}_{e,(k)}$), it is assumed that both signals are injected through the lower waveguide, yet in opposite directions. This will be the case for the add-drop filter design to follow, for reasons that will be made evident in the next section. Finally, the bulk materials are considered as nearly lossless; otherwise, an extra cavity photon lifetime term has to be introduced to account for the corresponding ohmic loss of the resonator.

CMT studies the temporal evolution of the field amplitudes $a_{(k)}$ and the output wave amplitudes $s_{\mathrm{th},(k)}/s_{\mathrm{dr},(k)}$ at the through and drop ports, respectively, for each signal. Therefore, the nonlinear terms appearing should be expressed in terms of the cavity amplitudes $a_{(k)}$ rather than the electric field values, which are spatially-varying across the resonator. Regarding the SPM/XPM nonlinear terms, this can be achieved by defining the γ_{SPM} and γ_{XPM} coefficients (measured in $\mathrm{W}^{-1}\mathrm{s}^{-2}$),[48] expressing the nonlinear shifts as

$$\Delta\omega_{\mathrm{SPM},(k)} = -\gamma_{\mathrm{SPM},(k)}|a_{(k)}|^2, \tag{9a}$$

$$\Delta\omega_{\mathrm{XPM},(k\ell)} = -2\gamma_{\mathrm{XPM},(k\ell)}|a_{(\ell)}|^2. \tag{9b}$$

In our formulation, the linear graphene-related terms are divided to the intraband and the interband contributions, given by Eqs. (4) and (5), respectively. The intraband terms do not depend on the field amplitude of the cavity; thus, they are constant over time. The interband terms need an appropriate normalization in order to disentangle the temporal and spatial dependance of the electric and magnetic field quantities. This is achieved by introducing the reference fields $\mathbf{E}_{\mathrm{ref},(k)}$ and $\mathbf{H}_{\mathrm{ref},(k)}$, having the fundamental property that $|a_{\mathrm{ref},(k)}|^2 = 1$,[34] which normalize the actual fields as $\{\mathbf{E}_{(k)}, \mathbf{H}_{(k)}\} = \{a_{(k)}\mathbf{E}_{\mathrm{ref},(k)}, a_{(k)}\mathbf{H}_{\mathrm{ref},(k)}\}$, indeed disentangling space and time dependencies. Under the above normalization, Eqs. (5) are transformed into

$$\Delta\omega_{\mathrm{SA},(k)} = -\frac{1}{4}\iint_S \sigma_{\mathrm{inter,Im}}(a_{(c)}\mathbf{E}_{\mathrm{ref},\parallel,(c)})|\mathbf{E}_{\mathrm{ref},\parallel,(k)}|^2\mathrm{d}S, \tag{10a}$$

$$\frac{1}{\tau_{\mathrm{SA},(k)}} = \frac{1}{4}\iint_S \sigma_{\mathrm{inter,Re}}(a_{(c)}\mathbf{E}_{\mathrm{ref},\parallel,(c)})|\mathbf{E}_{\mathrm{ref},\parallel,(k)}|^2\mathrm{d}S. \tag{10b}$$

Although this paper specifically focus on graphene, Eqs. (10) are expressed in a general form, allowing other 2D conductive materials exhibiting SA to be handled. The analysis gets specific only after plugging Eqs. (2) in Eqs. (10). Furthermore, it is useful to define the SA lifetime at very low control signal power $\tau^{(0)}_{\mathrm{SA},(k)} = \tau_{\mathrm{SA},(k)}(a_{(c)} \to 0)$, naturally corresponding to the cavity photon lifetime owing to the unsaturated interband loss.

The main CMT rate equations can be expressed in an easier to handle way, which also allows for better insight into the relative strength of each effect. A slowly varying envelope is assumed for the cavity amplitudes and the input waves, taking the form $a_{(k)} = \tilde{a}_{(k)}\exp\{j\omega^{\mathrm{op}}_{(k)}t\}$ and $s_{(k)} = \tilde{s}_{(k)}\exp\{j\omega^{\mathrm{op}}_{(k)}t\}$, where $\omega^{\mathrm{op}}_{(k)}$ is the operating frequency of the (k) wave, and the time is normalized as $t' = t/\tau^{(0)}_{\mathrm{SA},(p)}$. Under these substitutions, Eqs. (8a) become for the probe and control waves[48]

$$\frac{\mathrm{d}\tilde{a}_{(p)}}{\mathrm{d}t'} = j\left[-\delta_{(p)} + \delta_{\mathrm{intra},(p)} + \delta_{\mathrm{SA},(p)}(\tilde{a}_{(c)}) + \delta_{\mathrm{XPM},(pc)}(\tilde{a}_{(c)})\right]\tilde{a}_{(p)} - \left[r_{\mathrm{intra},(p)} + r_{\mathrm{SA},(p)}(\tilde{a}_{(c)}) + r_{\mathrm{rad},(p)} + r^{\mathrm{low}}_{e,(p)} + r^{\mathrm{upp}}_{e,(p)}\right]\tilde{a}_{(p)} + j\sqrt{2r^{\mathrm{low}}_{e,(p)}\tau^{(0)}_{\mathrm{SA},(p)}}\,\tilde{s}_{\mathrm{in},(p)}, \tag{11a}$$

$$\frac{\mathrm{d}\tilde{a}_{(c)}}{\mathrm{d}t'} = j\left[-\delta_{(c)} + \delta_{\mathrm{intra},(c)} + \delta_{\mathrm{SA},(c)}(\tilde{a}_{(c)}) + \delta_{\mathrm{SPM},(c)}(\tilde{a}_{(c)})\right]\tilde{a}_{(c)} - \left[r_{\mathrm{intra},(c)} + r_{\mathrm{SA},(c)}(\tilde{a}_{(c)}) + r_{\mathrm{rad},(c)} + r^{\mathrm{low}}_{e,(c)} + r^{\mathrm{upp}}_{e,(c)}\right]\tilde{a}_{(c)} + j\sqrt{2r^{\mathrm{low}}_{e,(c)}\tau^{(0)}_{\mathrm{SA},(p)}}\,\tilde{s}_{\mathrm{in},(c)}, \tag{11b}$$

where $\delta = \tau^{(0)}_{\mathrm{SA},(p)}\Delta\omega$ are the normalized frequency detunings and $r = \tau^{(0)}_{\mathrm{SA},(p)}/\tau$ are the normalized loss ratios for the different decay mechanisms present, both of which may depend on the cavity amplitude $\tilde{a}_{(c)}$ of the strong control wave. For the unperturbed resonance, it is noted that $\delta_{(k)} = \tau^{(0)}_{\mathrm{SA},(p)}(\omega^{\mathrm{op}}_{(k)} - \omega_{(k)})$.

III. DESIGN RULES FOR SA-DRIVEN ADD-DROP FILTERS

Having established the nonlinear framework that describes the resonant system under study, we step forward by presenting in this section the operation principles of the proposed routing element. Specifically, we aim to extract design rules that point out how to determine the coupling conditions between the cavity and the two feeding waveguides, in order to access high performance metrics.

To this goal, we simplify the original CMT equations by ignoring the perturbation-induced resonance frequency shift terms and retain only the loss mechanism associated to the SA-affected interband absorption and the coupling terms to the access waveguides (i.e., we set $\delta_{\mathrm{intra}} = \delta_{\mathrm{SA}} = \delta_{\mathrm{SPM}} = \delta_{\mathrm{XPM}} = 0$ and $r_{\mathrm{intra}} = r_{\mathrm{rad}} = 0$). Under the above simplifications and when the system is fed by a single wave carried by the lower waveguide, as in Fig. 2, the transmission expressions at the through and the drop ports under CW conditions acquire the form,

$$T_{\mathrm{th}} = \frac{(r_{\mathrm{SA}} + r^{\mathrm{upp}}_e - r^{\mathrm{low}}_e)^2 + \delta^2}{(r_{\mathrm{SA}} + r^{\mathrm{upp}}_e + r^{\mathrm{low}}_e)^2 + \delta^2}, \tag{12a}$$

$$T_{\mathrm{dr}} = \frac{4r^{\mathrm{upp}}_e r^{\mathrm{low}}_e + \delta^2}{(r_{\mathrm{SA}} + r^{\mathrm{upp}}_e + r^{\mathrm{low}}_e)^2 + \delta^2}, \tag{12b}$$

respectively, with $r_{\mathrm{SA}} = \tau^{(0)}_{\mathrm{SA}}/\tau_{\mathrm{SA}}$. On resonance ($\delta = 0$), complete extinction of transmission for the through port can be obtained when $r_{\mathrm{SA}} + r^{\mathrm{upp}}_e = r^{\mathrm{low}}_e$, a condition known as *critical coupling*. On the contrary, a similar condition does not apply to the drop port, at which a fraction of the outgoing power always ends up. Given that r_{SA} can be dynamically controlled (either in a self-effect or using a separate optical control wave of sufficient intensity), the critical coupling condition can be selectively met, guiding a considerable portion of the input power to the drop port; we refer to this as *state* (2), where $T^{(2)}_{\mathrm{th}} = 0$ and $T^{(2)}_{\mathrm{dr}} = r^{\mathrm{upp}}_e/r^{\mathrm{low}}_e$. On the other hand, when critical coupling is not met, the injected power ends up at both through and drop ports. For the optimum performance of a routing element in this state, the power ending up at the through port has to be maximized, and this will be the case in the absence of SA; in that case $r_{\mathrm{SA}} = 1$, taking its largest achievable value. We refer to this as *state* (1) and denote the respective CW transmissions as $T^{(1)}_{\mathrm{th}}$ and $T^{(1)}_{\mathrm{dr}}$.

The proposed routing element cannot perform ideally, mostly because of the drop port inherent restrictions, that always result in a finite extinction ratio (ER). Nonetheless, one can determine a specific range for the parameters r^{upp}_e and r^{low}_e where the device can demonstrate satisfactory performance. For this work, we set the following four design rules: (*i*) acceptable insertion loss, IL $\leq \mathcal{L}$ dB (or L in terms of dimensionless transmission), for both ports, (*ii*) approximately equal high transmission at both states, $T^{(1)}_{\mathrm{th}} \approx T^{(2)}_{\mathrm{dr}}$, differing by maximum 2 dB, (*iii*) high extinction ratio at the drop port, $\mathrm{ER}_{\mathrm{dr}} \geq 10$ dB, and (*iv*) $r^{\mathrm{low}}_e > r^{\mathrm{upp}}_e$, set by the critical coupling condition since $0 \leq r_{\mathrm{SA}} \leq 1$. It is reiterated that critical coupling ensures that $\mathrm{ER}_{\mathrm{th}}$ will be infinite, which is the ideal case.

Rule (*i*) sets two conditions that the loss ratios for the external lifetimes τ_e corresponding to coupling to the lower/upper waveguides have to meet, namely $r^{\mathrm{low}}_e \leq (1/L)r^{\mathrm{upp}}_e$ and $r^{\mathrm{low}}_e \leq [(1-\sqrt{L})/(1+\sqrt{L})](r^{\mathrm{upp}}_e + 1)$, obtained by seeking for $T^{(2)}_{\mathrm{dr}} \geq L$ and $T^{(1)}_{\mathrm{th}} \geq L$, respectively. The latter inequality, when combined with rule (*iv*), results in the extra condition $r^{\mathrm{upp}}_e \leq (1-\sqrt{L})/(2\sqrt{L})$. Thus, the loss ratios for external coupling must fulfil

$$r^{\mathrm{upp}}_e \in \left(0,\ \frac{1-\sqrt{L}}{2\sqrt{L}}\right], \tag{13a}$$

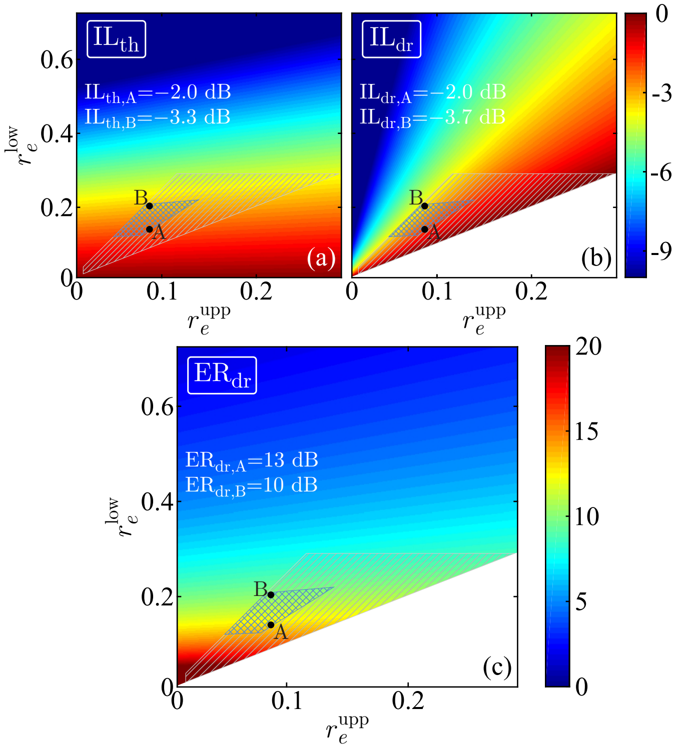

FIG. 3. Routing element performance evaluation in the r_e^{upp}–r_e^{low} space. (a), (b) IL in the through and drop ports, respectively. (c) ER in drop port. Inside the single-hatched gray areas, the restrictions of Eqs. (13) are met, when $\mathcal{L} = 4$ dB. Inside the blue cross-hatched regions, where all four design rules are met, the device exhibits notable performance. The blank regions in (b) and (c) are physically unreachable due to the critical coupling condition that is met for extracting the results ($r_e^{\mathrm{low}} > r_e^{\mathrm{upp}}$).

$$r_e^{\mathrm{low}} \in \left[r_e^{\mathrm{upp}},\ \min\left\{ \frac{1}{L} r_e^{\mathrm{upp}},\ \frac{1-\sqrt{L}}{1+\sqrt{L}} (r_e^{\mathrm{upp}} + 1) \right\} \right]. \tag{13b}$$

The restrictions of Eqs. (13) set the limits for both output ports to have acceptable IL and allow the system to fulfill the critical coupling condition.

To better illustrate how all four rules are met, we perform a parametric investigation in the $r_e^{\mathrm{upp}} - r_e^{\mathrm{low}}$ space. The results are depicted in Fig. 3 for the insertion loss [Figs. 3(a), (b)] in both ports and the extinction ratio in the drop port [Figs. 3(c)]. In the single-hatched gray areas the restrictions of Eqs. (13) are met, when the parameter for maximum tolerable insertion losses bas been set to $\mathcal{L} = 4$ dB, and it is evident that both ports restrain IL below the limit $\mathcal{L}$. All four design rules are simultaneously fulfilled inside the light blue cross-hatched boxes, thus resulting in acceptable performance with respect to insertion loss and extinction ratio, in both ports. We note here that the areas with no color in Figs. 3(b), (c), where $r_e^{\mathrm{low}} < r_e^{\mathrm{upp}}$, are physically unreachable since the critical coupling condition that provides the high output in the drop port requests that $r_e^{\mathrm{low}} > r_e^{\mathrm{upp}}$.

The specific choice of the operation point inside the blue cross-hatched region still affects the power level that is required to meet the critical coupling condition, owing to SA. When $r_e^{\mathrm{low}} \sim r_e^{\mathrm{upp}}$, the critical coupling condition is met for $r_{\mathrm{SA}} \to 0$, which translates to increased injected power. On the other hand, when r_e^{low} significantly exceeds r_e^{upp}, the critical coupling condition is met for an increased value of r_{SA}, thus requiring less injected power. This is better highlighted by the two possible operating points, marked as A and B in Fig. 3. For point A $\mathrm{IL_{th,A}} = \mathrm{IL_{dr,A}} = -2$ dB and $\mathrm{ER_{dr,A}} = 13$ dB; however, the power that is required to reach the critical coupling is more than four times greater compared to the one required for operation at point B with $\mathrm{IL_{th,B}} = -3.3$ dB, $\mathrm{IL_{dr,B}} = -3.7$ dB and $\mathrm{ER_{dr,B}} = 10$ dB. This is a consequence of the critical coupling condition, setting $r_{\mathrm{SA,A}} = r_e^{\mathrm{low}} - r_e^{\mathrm{upp}} = 0.05$ for point A. In contrast, the respective requirement for point B is $r_{\mathrm{SA,B}} = 0.12$, which has moved closer to the value $r_{\mathrm{SA}} = 1$ that denotes the absence of SA, and thus naturally requires a lower power level in comparison to point A.

The above explicit design rules are essential for achieving a high-performance resonant system, intended for sophisticated SA operations. These design rules have been extracted for a simplified system without perturbation-induced resonance frequency shifts and other loss mechanisms. This approach does not restrict their general applicability since the additional, initially ignored terms, can be integrated either with δ or with the r_e^{upp} parameters, impacting the overall performance. This statement will become clearer in the following section, which focuses to the presentation of the physical system.

IV. GRAPHENE-ENHANCED SILICON DISK RESONATOR AS ROUTING ELEMENT

Having presented the general design strategy in the preceding section, we are now in position to propose an all-optical resonant system that can selectively route an incoming guided mode to two different exit ports. The physical system is depicted in Fig. 4(a), consisting of a silicon disk resonator with radius R, that is further silica-cladded. Two straight waveguides with cross-sectional dimensions $w \times h = 200 \times 340$ nm^2 are used as the access ports of the system, having coupling distances g_{low} and g_{upp}, respectively. A graphene sheet is laid on top of the planar structure, providing the loss-saturation mechanism that is necessary for the all-optical control of the resonant element. For efficient light-graphene interaction, transverse magnetic (TM) polarization is preferred because of the strong azimuthal component [Figs. 4(b), (c)], which apart of being tangential to the graphene sheet is also maximized on top of the cavity.[38] Working with the fundamental TM mode justifies the cross-section dimensions chosen for the waveguides, as well.

The refractive indices for the materials involved are set to $n_{\mathrm{Si}} = 3.48$ and $n_{\mathrm{SiO_2}} = 1.45$,[51] considering mate-

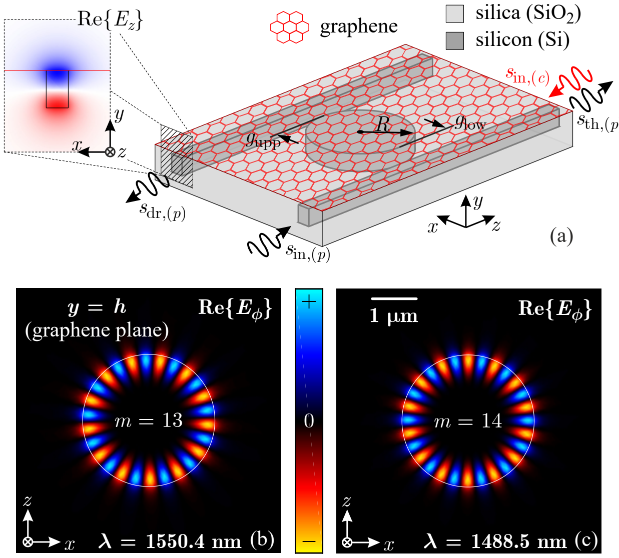

FIG. 4. (a) Perspective view of the proposed graphene-enhanced silicon disk resonator. Inset: Out-of-plane electric field component, Re$\{E_z\}$, of the supported TM mode, strongly interacting with graphene. (b), (c) Azimuthal electric field distribution, Re$\{E_\phi\}$, for resonant modes of order $m = 13$ and $m = 14$, respectively, recorded on the graphene plane.

TABLE I. Resonance characteristics, wavelength and quality factors, of the two resonant modes under consideration.

	Probe ($m = 13$)	Control ($m = 14$)
$\lambda_{(k)}$	1550.4 nm	1488.5 nm
Q_{rad}	$49,300$	$169,000$
Q_{intra}	$200,000$	$260,000$
$Q_{\text{SA}}^{(0)}$	960	$1,072$
Q_e^{low}	$4,829$	$9,093$
Q_e^{upp}	$10,536$	$22,143$

rial dispersion as negligible. The Kerr effect is accounted for in both silicon and silica, with the respective nonlinear indices being $n_2^{\text{Si}} = 2.5 \times 10^{-18}$ m^2/W and $n_2^{\text{SiO}_2} = 2.6 \times 10^{-20}$ m^2/W.[52,53] Linear properties of graphene are given by Eq. (1) and the third-order nonlinear response (Kerr effect) is associated with the nonlinear surface conductivity[12] equal to $\sigma_3 = -j1.2 \times 10^{-20}$ S(m/V)^2. Finally, we do not account for TPA and FCEs in silicon, as our preliminary simulations have proved that they are negligible at the examined power levels.

The resonator radius is selected so that the respective radiation quality factors, calculated using appropriate uncoupled eigenvalue simulations,[43] are sufficiently high, meaning that minimal radiation leaks out of the resonator. Amongst others, low radiation loss is beneficial for accessing the critical coupling condition at low input power. That is because r_{rad} is grouped together with r_e^{upp} when the critical coupling condition is assessed, thus forcing the latter to approach r_e^{low}; this will subsequently raise the power requirements for critical coupling, as already explained in Sec. III. The same is also true for the non-saturated losses of graphene (i.e., intraband absorption r_{intra}), but this parameter cannot be engineered, while it is expected to have a small contribution. Taking all of the above into consideration, a radius of $R = 1.503$ μm is chosen, so that $Q_{\text{rad},(k)}$ is in the range of 50,000. Subsequently, the coupling gaps are determined following the rules presented in Sec. III. With respect to Fig. 3, point B is preferred due to the reduced power requirements, though the exact r_e values are slightly altered to account for the extra loss terms present. Ultimately, the two gaps are specified using coupled eigenvalue simulations and are found equal to $g_{\text{low}} = 348$ nm and $g_{\text{upp}} = 414$ nm, with the higher value for g_{upp} reflecting the necessary condition $r_e^{\text{low}} > r_e^{\text{upp}}$.

The system's linear characterization has been performed by conducting finite-element eigenvalue simulations using COMSOL Myltiphysics®, including both the uncoupled resonator and the resonator coupled to the access waveguides. Two modes are considered: the mode of order $m = 13$, corresponding to the low-power probe wave, and the mode of order $m = 14$, corresponding to the high-power control wave. This placement is preferred since it allows the SA induced by the control wave to affect the loss that the probe wave experiences.[35,54] The resonance characteristics of the two modes are summarized in Table I, including a quality factor breakdown in different loss channels. The choice of power injection through the lower waveguide becomes now evident; a Q_e value as close to $Q_{\text{SA}}^{(0)}$ as possible results in higher coupling efficiency for the same input power level. The normalized parameters appearing in the CMT equations (i.e. loss ratios and detunings) are obtained in a post-processing step from the linear simulations and are gathered in Table II. We must note that all power-dependent parameters are calculated for $P_{\text{in},(c)} = 9$ mW, which is the necessary input power for the routing element to redirect the input probe wave from the through to the drop port at the critical coupling condition, as it will become evident below.

The introduction of the normalized coefficients in the CMT framework allows for the evaluation of the proposed

TABLE II. Normalized quantities introduced in the CMT framework. All power-dependent quantities correspond to $P_{\text{in},(c)} = 9$ mW.

	Probe ($m = 13$)	Control ($m = 14$)
r_{rad}	0.019	0.006
r_{intra}	0.005	0.004
r_e^{low}	0.199	0.118
r_e^{upp}	0.091	0.048
δ_{intra}	$+0.057$	$+0.050$
δ_{SPM} (9 mW)	$\to 0$	$+0.066$
δ_{XPM} (9 mW)	$+0.142$	$\to 0$
δ_{SA} (9 mW)	-0.215	-0.203

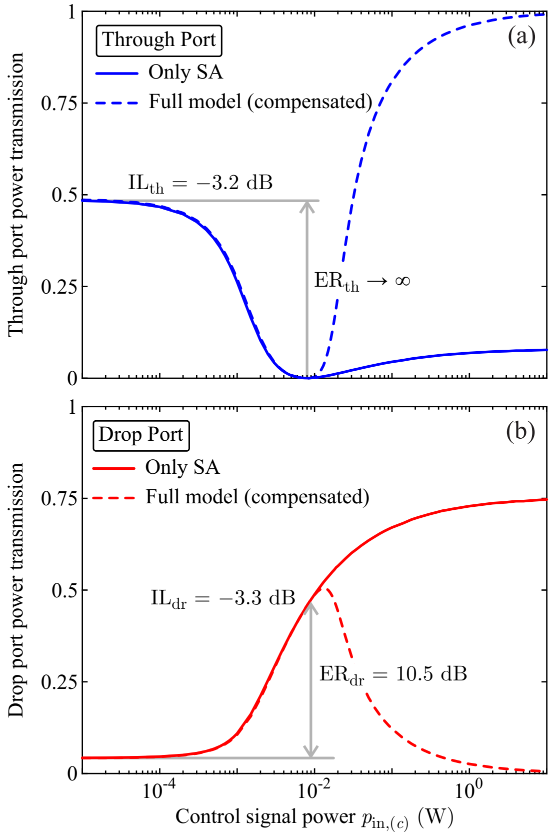

FIG. 5. CW transmission obtained with the CMT framework, using the parameters reported in Table II. Solid lines correspond the case where loss saturation is the only effect taking place, whereas dashed lines correspond to the full case that all nonlinear effects are introduced. (a) Through port transmission and (b) drop port transmission. IL in both ports are tolerable (approximately −3 dB) while the drop port enjoys a satisfactory $\mathrm{ER_{dr}}$ of 10.5 dB.

routing element. At first, we study the CW response of the system by solely examining the loss saturation effect. The results are depicted in Fig. 5 (solid lines) for the through and the drop port transmission. Initially, the through port transmission is high ($\mathrm{IL_{th}} = -3.2$ dB) and only a marginal fraction of the probe wave ends up in the drop port. When the strong control signal is applied, the through port transmission starts to drop, until it zeroes out for $P_{\mathrm{in},(c)} = 9$ mW; the critical coupling condition has been met. Simultaneously, the drop transmission raises monotonically, reaching at the above power level $\mathrm{IL_{dr}} = -3.3$ dB and $\mathrm{ER_{dr}} = 10.5$ dB. The performance metrics are well in accordance with the analysis of Sec. III. For higher control signal powers, the drop port performance further improves but $\mathrm{ER_{th}}$ deviates from its optimum value ($\to \infty$), given that critical coupling condition has been trespassed.

The previous performance can be considered as the ideal one, because all other linear and nonlinear effects have been artificially switched off. Still, incorporating them is not necessarily distractive. Despite the fact that not much can be done for the extra loss factors introduced, the resonance frequency shift terms can be cancelled out by wisely choosing the operating frequencies $\omega^{\mathrm{op}}_{(k)}$. More specifically, by choosing the normalized detuning parameters as $\delta_{(k)} = \delta_{\mathrm{intra},(k)} + \delta_{\mathrm{SA},(k)} + \delta_{\mathrm{SPM},(k)} + \delta_{\mathrm{XPM},(k\ell)}$, the frequency detuning terms in Eq. (11) vanish. It is important to note that in the determination of the operating frequencies we should exercise extra care, since the parameters $\delta_{\mathrm{SA},(k)}$, $\delta_{\mathrm{SPM},(k)}$, and $\delta_{\mathrm{XPM},(k\ell)}$ all depend on the control wave power. This is the reason that their values, reported in Table II, are calculated for the targeted operating input power $P_{\mathrm{in},(c)} = 9$ mW. Ultimately, the detuning parameters are set to $\delta_{(p)} = -0.016$ and $\delta_{(c)} = -0.087$, corresponding to the operating wavelengths $\lambda^{\mathrm{op}}_{(p)} = 1550.41$ nm and $\lambda^{\mathrm{op}}_{(c)} = 1488.56$ nm, respectively, slightly different from the respective resonant wavelengths of Table I. This is a direct consequence of the counteraction between the negative interband-induced resonance frequency shift (SA related) and the positive Kerr- and intraband-induced shifts.

Incorporating all linear and nonlinear effects in the CMT equations, together with the frequency detunings determined above, results in transmission curves imprinted with dashed lines in Fig. 5. Up to the operating power of 9 mW, the simplified approach (SA only) and the compensated full model are practically identical. On the other hand, for higher control wave powers the two approaches deviate substantially. This is attributed to the fact that the compensation is no longer sufficient due to the dependency of $\delta_{\mathrm{SA},(k)}$, $\delta_{\mathrm{SPM},(k)}$, and $\delta_{\mathrm{XPM},(k\ell)}$ terms on the control signal input power, thus rendering the overall detuning nonzero again. Nevertheless, the linearly and nonlinearly induced frequency shifts can be canceled up until the operating power, allowing for the routing element to achieve the design performance metrics. Such a complex response is computationally available due to our CMT framework and possibly could not have been accessible with full-wave nonlinear simulations in particular under pulsed conditions, due to the excessive computational burden. We note here that, as Fig. 5(b) indicates, the optimum operating point for the $\mathrm{ER_{dr}}$ requires a somehow higher input power of the control wave. However, we do not opt for working at this point, mostly because of the impairment in the $\mathrm{ER_{th}}$ that will entail.

The maximum bandwidth of the proposed element can be found by resorting to the solution of the temporal form of the CMT equations [Eq. (11)]. To gradually introduce the routing concept, we inject a low-power probe wave, encoded with the bitstream sequence 101101 at a 10 Gbps line rate. Each ”1” bit is shaped with a fourth order Super-Gaussian pulse with full-width at half-maximum (FWHM) equal to 60% of the bit duration and a peak power equal to 1 μW. According to the results shown in Fig. 6(a), the first three bits, where no control signal is applied, end up out of the through port, exhibiting the expected $\mathrm{IL_{th}} = -3.2$ dB. For the next three bits, a strong CW control signal is also injected in the

PLEASE CITE THIS ARTICLE AS DOI: 10.1063/5.0004552

resonator, with its power being equal to 9 mW, as already assessed from the CW analysis. The control signal saturates graphene losses, fulfilling the critical coupling condition and thus allowing the probe wave to end up in the drop port, also with the expected $\mathrm{IL}_{\mathrm{dr}} = -3.3$ dB. The dynamic behaviour reveals some secondary transient effects, such as the small peaks seen in the through port transmission for the 4th and 6th bit, but if sampling is performed at the center of each time slot, the anticipated extinction ratios are $\mathrm{ER}_{\mathrm{th}} = 45$ dB (almost infinite) and $\mathrm{ER}_{\mathrm{dr}} = 10.5$ dB.

In a more realistic approach, the control signal is also pulsed, here exemplified in the form of a 010101 bitstream, with "1" bits represented by the same type of pulse as for the probe wave but with 9 mW peak power. Under these control conditions, every other probe bit should leave the resonator from the drop port. This scenario is depicted in Fig. 6(b). Bits exiting from the through port are identical to those of the previous case, given that the loss saturation effect is absent ($P_{\mathrm{in},(c)} = 0$). For the remaining bits, some distortion in the shape of the output pulses is observed, owing to the gradual filling of the cavity with the control light that subsequently establishes SA with some delay. Despite these small discrepancies, the overall pulsed performance is relatively unchangeable.

Since the above-discussed distortion is a product of the slow response of the cavity, a rational approach is to inject the control wave bitstream with a small time offset in advance.[33] This is the case depicted in Fig. 6(c), where the control wave bitstream is pre-shifted in time by 14 ps (14% of the bit duration), allowing for the SA to timely establish. The introduced time pre-shift restores the shape of the output waveforms, simultaneously suppressing the appearing side-lobes to their amplitude level under CW control conditions. It is noted that the previous probe bit is not affected, since the duty cycle of the input stream is chosen to allow for such pre-shifting levels. Overall, the performance metrics are the same as in Fig. 6(a).

As a final example, we increase the bitstream rate to 20 Gbps and evaluate the routing performance. For the results depicted in Fig. 6(d), we have already introduced the appropriate time pre-shifting of the control signal (also here equal to 14 ps or 28% of the bit duration). The time pre-shifting cannot restore the shape of the drop port pulses, which now does not present a flat-top at pulse center, or adequately suppress the side-lobes seen in the through port. Furthermore, the introduced pre-shifting starts affecting the previous bit, though in a mild way. Despite the above, even for this high rate, the performance metrics are mostly maintained. For higher bitstreams rates though, both $\mathrm{IL}_{\mathrm{dr}}$ and $\mathrm{ER}_{\mathrm{dr}}$ will be significantly reduced. Given that when the control wave is switched off the probe pulse shape is maintained, the restrictive factor appears to be the energy of the control pulse, which is repressed due to the reduced pulse width, and the finite cavity lifetime. Thus, although the 20 Gbps seems to be the upper speed limit for this specific routing device, a control pulse with more appropriate energy distribution or higher duty cycle might allow for even higher bandwidths. Alternatively, seeking for cavities with lower quality factors, which inherently result in faster responses might be an option, at the expense of higher peak power requirements for the control signal.

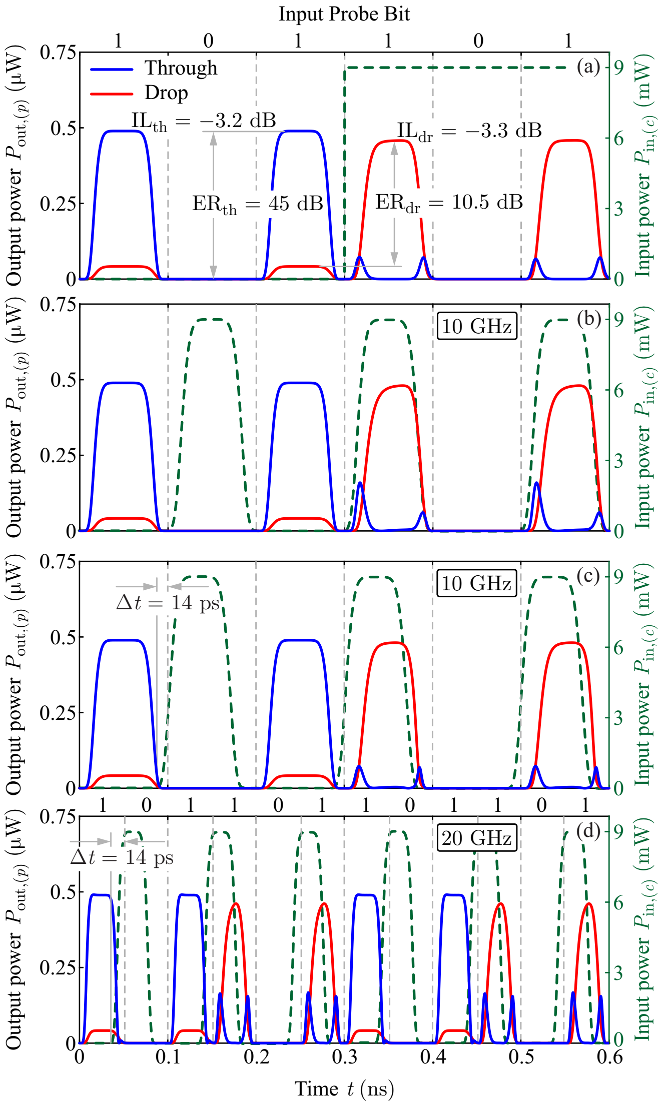

FIG. 6. Dynamic response of the proposed routing element. The examined probe bit sequence is 101101, consisting of fourth order Super-Gaussian pulses with a peak power of 1 μW and FWHM equal to 60% of the bit duration. (a) Ideal routing of a 10 Gbps bitstream under CW control signal injection. (b) Routing of a 10 Gbps bitstream under pulsed control signal injection; pulse distortion is now evident. (c) Routing of a 10 Gbps bitstream under time-shifted pulsed control signal injection. Pulse distortion has now been suppressed to a high extent. (d) Routing of a 20 Gbps bitstream under time-shifted pulsed control signal injection. Side peaks and pulse distortion are more pronounced, setting the bandwidth upper limit of the routing element.

Journal of Applied Physics ACCEPTED MANUSCRIPT
This is the author's peer reviewed, accepted manuscript. However, the online version of record will be different from this version once it has been copyedited and typeset.
PLEASE CITE THIS ARTICLE AS DOI: 10.1063/5.0004552

V. CONCLUSION

In conclusion, we have proposed a simple and practical all-optical resonant routing element. The resonant device is designed on the standard silicon-on-insulator platform, further enhanced by a uniform graphene layer that provides the necessary loss saturation mechanism for the all-optical control. Graphene loss saturation is nowadays admitted as a mature nonlinear effect accessed at rather low power levels, and following the early successful applications in fiber lasers it is now finding its way to nanophotonics. Our investigations revealed a very moderate control power level of 9 mW, especially appealing for contemporary nonlinear nanophotonic devices, while the device bandwidth of 20 GHz covers a broad range of practical applications, the most anticipated of which is its use as a multiplexer/demultiplexer in an optical time-domain multiplexing (OTDM) system; such an action is well established through the results of Fig. 6. Other possible applications might be an all-optical switch [Fig. 6(a)] or an all-optical modulator. In the latter two applications that are in principle quite similar, only the through port is considered as the output while the light ending up in the drop port is assumed to impinge on a matched load and it is safely ignored.

The computational framework developed to analyze the presented resonant system is a versatile tool, suitable for a broad range of nonlinear nanophotonic devices. As demonstrated, it can efficiently handle multichannel nonlinear effect such as SA, cross-SA, and self- and cross-phase modulation, simultaneously providing with the physical insight associated to each effect. Finally, it allows for the extraction of elegant design rules that can provide a reliable path when targeting the realization of practical nonlinear resonant devices, capable of meeting real-world specifications.

DATA AVAILABILITY

The data that support the findings of this study are available from the corresponding author upon reasonable request.

ACKNOWLEDGMENTS

The research work was supported by the Hellenic Foundation for Research and Innovation (H.F.R.I.) under the "First Call for H.F.R.I. Research Projects to support Faculty members and Researchers and the procurement of high-cost research equipment grant." (Project Number: HFRI-FM17-2086)

[1] K. S. Novoselov, V. I. Fal'ko, L. Colombo, P. R. Gellert, M. G. Schwab, and K. Kim, Nature **490**, 192 (2012).
[2] P. Avouris, Nano Letters **10**, 4285 (2010).
[3] M. Romagnoli, V. Sorianello, M. Midrio, F. H. L. Koppens, C. Huyghebaert, D. Neumaier, P. Galli, W. Templ, A. D'Errico, and A. C. Ferrari, Nature Reviews Materials **3**, 392 (2018).
[4] J. Wang, Z. Cheng, and X. Li, Advances in Condensed Matter Physics **2018**, 9324528 (2018).
[5] L. Wang, X. Zhou, S. Yang, G. Huang, and Y. Mei, Photonics Research **7**, 905 (2019).
[6] H. wen Shu, M. Jin, Y. sheng Tao, and X. jun Wang, Frontiers of Information Technology & Electronic Engineering **20**, 458 (2019).
[7] Z. Lu and W. Zhao, Journal of the Optical Society of America B **29**, 1490 (2012).
[8] Y. Wan and L. Deng, Journal of Applied Physics **121**, 163102 (2017).
[9] G. Sinatkas, T. Christopoulos, O. Tsilipakos, and E. E. Kriezis, Physical Review Applied **12**, 064023 (2019).
[10] G. Demetriou, H. T. Bookey, F. Biancalana, E. Abraham, Y. Wang, W. Ji, and A. K. Kar, Optics Express **24**, 13033 (2016).
[11] E. Dremetsika, B. Dlubak, S.-P. Gorza, C. Ciret, M.-B. Martin, S. Hofmann, P. Seneor, D. Dolfi, S. Massar, P. Emplit, and P. Kockaert, Optics Letters **41**, 3281 (2016).
[12] K. Alexander, N. A. Savostianova, S. A. Mikhailov, D. V. Thourhout, and B. Kuyken, ACS Photonics **5**, 4944 (2018).
[13] S. Yamashita, APL Photonics **4**, 034301 (2019).
[14] C. Yadav and S. Roy, Journal of Computational Electronics **14**, 209 (2014).
[15] T. Christopoulos, O. Tsilipakos, and E. E. Kriezis, Journal of Applied Physics **122**, 233101 (2017).
[16] A. Kar, N. Goswami, and A. Saha, Applied Optics **56**, 2321 (2017).
[17] D. Zhao, S. Ke, Y. Hu, B. Wang, and P. Lu, Journal of the Optical Society of America B **36**, 1731 (2019).
[18] G. Wang, A. A. Baker-Murray, and W. J. Blau, Laser & Photonics Reviews **13**, 1800282 (2019).
[19] A. Marini, J. D. Cox, and F. J. G. de Abajo, Physical Review B **95**, 125408 (2017).
[20] Q. Bao, H. Zhang, Z. Ni, Y. Wang, L. Polavarapu, Z. Shen, Q.-H. Xu, D. Tang, and K. P. Loh, Nano Research **4**, 297 (2011).
[21] A. Malouf, O. Henderson-Sapir, S. Set, S. Yamashita, and D. J. Ottaway, Applied Physics Letters **114**, 091111 (2019).
[22] Z. Sun, T. Hasan, F. Torrisi, D. Popa, G. Privitera, F. Wang, F. Bonaccorso, D. M. Basko, and A. C. Ferrari, ACS Nano **4**, 803 (2010).
[23] D. Popa, Z. Sun, T. Hasan, F. Torrisi, F. Wang, and A. C. Ferrari, Applied Physics Letters **98**, 96 (2011).
[24] D. I. M. Zen, N. Saidin, S. S. A. Damanhuri, S. W. Harun, H. Ahmad, M. A. Ismail, K. Dimyati, A. Halder, M. C. Paul, S. Das, M. Pal, and S. K. Bhadra, Applied Optics **52**, 1226 (2013).
[25] C. A. Zaugg, Z. Sun, V. J. Wittwer, D. Popa, S. Milana, T. Kulmala, R. S. Sundaram, M. Mangold, O. D. Sieber, M. Golling, Y. Lee, J. H. Ahn, A. C. Ferrari, and U. Keller, Optics Express **21**, 739 (2013).
[26] M. Takahashi, W. Ueda, N. Goto, and S. Yanagiya, IEEE Photonics Journal **5**, 6602109 (2013).
[27] Y. Meng, L. Deng, Z. Liu, H. Xiao, X. Guo, M. Liao, A. Guo, T. Ying, and Y. Tian, Optics Express **25**, 18451 (2017).
[28] K. Alexander, Y. Hu, M. Pantouvaki, S. Brems, I. Asselberghs, S.-P. Gorza, C. Huyghebaert, J. V. Campenhout, B. Kuyken, and D. V. Thourhout, in *CLEO: 2015* (2015) p. STh4H.7.
[29] P. Demongodin, H. E. Dirani, J. Lhuillier, R. Crochemore, M. Kemiche, T. Wood, S. Callard, P. Rojo-Romeo, C. Sciancalepore, C. Grillet, and C. Monat, APL Photonics **4**, 076102 (2019).
[30] H. Wang, N. Yang, L. Chang, C. Zhou, S. Li, M. Deng, Z. Li, Q. Liu, C. Zhang, Z. Li, and Y. Wang, Photonics Research **8**, 468 (2020).
[31] J. Wang, L. Zhang, Y. Chen, Y. Geng, X. Hong, X. Li, and Z. Cheng, Applied Physics Express **12**, 032003 (2019).
[32] M. Ono, M. Hata, M. Tsunekawa, K. Nozaki, H. Sumikura, H. Chiba, and M. Notomi, Nature Photonics **14**, 37 (2020).

[33] P. Ma, H. Jackel, G.-L. Bona, and C. Hafner, IEEE Journal of Quantum Electronics **50**, 1 (2014).

[34] V. G. Ataloglou, T. Christopoulos, and E. E. Kriezis, Physical Review A **97**, 063836 (2018).

[35] Y. Y. Ren, M. Feng, K. Zhang, J. Yang, Y. Miao, F. F. Song, Z. B. Liu, and F. Song, Physica Scripta **94**, 125506 (2019).

[36] G. W. Hanson, IEEE Transactions on Antennas and Propagation **56**, 747 (2008).

[37] L. A. Falkovsky, Physics-Uspekhi **51**, 887 (2008).

[38] D. Chatzidimitriou, A. Pitilakis, and E. E. Kriezis, Journal of Applied Physics **118**, 023105 (2015).

[39] G. Xing, H. Guo, X. Zhang, T. C. Sum, and C. H. A. Huan, Optics Express **18**, 4564 (2010).

[40] A. Marini and F. J. G. de Abajo, Physical Review Letters **116**, 217401 (2016).

[41] J. Bravo-Abad, S. Fan, S. G. Johnson, J. D. Joannopoulos, and M. Soljacic, Journal of Lightwave Technology **25**, 2539 (2007).

[42] T. Christopoulos, O. Tsilipakos, N. Grivas, and E. E. Kriezis, Physical Review E **94**, 062219 (2016).

[43] T. Christopoulos, O. Tsilipakos, G. Sinatkas, and E. E. Kriezis, Optics Express **27**, 14505 (2019).

[44] M. Soljačić, M. Ibanescu, S. G. Johnson, Y. Fink, and J. D. Joannopoulos, Physical Review E **66**, 055601(R) (2002).

[45] M. F. Yanik, H. Altug, J. Vuckovic, and S. Fan, Journal of Lightwave Technology **22**, 2316 (2004).

[46] D. M. Ramirez, A. W. Rodriguez, H. Hashemi, J. D. Joannopoulos, M. Soljačić, and S. G. Johnson, Physical Review A **83**, 033834 (2011).

[47] O. Tsilipakos, T. Christopoulos, and E. E. Kriezis, Journal of Lightwave Technology **34**, 1333 (2016).

[48] T. Christopoulos, O. Tsilipakos, G. Sinatkas, and E. E. Kriezis, Physical Review B **98**, 235421 (2018).

[49] P. N. Butcher and D. Cotter, *The elements of nonlinear optics* (Cambridge University Press, Cambridge, 1990).

[50] N. Vermeulen, J. Cheng, J. E. Sipe, and H. Thienpont, IEEE Journal of Selected Topics in Quantum Electronics **22**, 347 (2016).

[51] B. Tatian, Applied Optics **23**, 4477 (1984).

[52] M. Dinu, F. Quochi, and H. Garcia, Applied Physics Letters **82**, 2954 (2003).

[53] D. Milam, Applied Optics **37**, 546 (1998).

[54] W. Li, B. Chen, C. Meng, W. Fang, Y. Xiao, X. Li, Z. Hu, Y. Xu, L. Tong, H. Wang, W. Liu, J. Bao, and Y. R. Shen, Nano Letters **14**, 955 (2014).

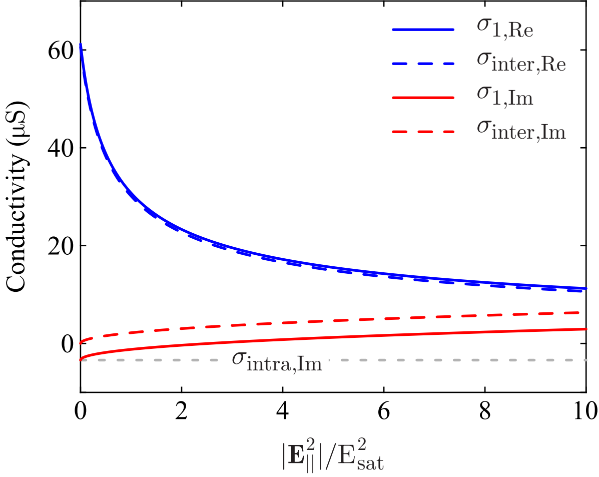
$\sigma_{1,\mathrm{Re}}$
$\sigma_{\mathrm{inter,Re}}$
$\sigma_{1,\mathrm{Im}}$
$\sigma_{\mathrm{inter,Im}}$
$\sigma_{\mathrm{intra,Im}}$
Conductivity (μS)
60
40
20
0
0
2
4
6
8
10
$|\mathbf{E}_{||}^2|/\mathrm{E}_{\mathrm{sat}}^2$

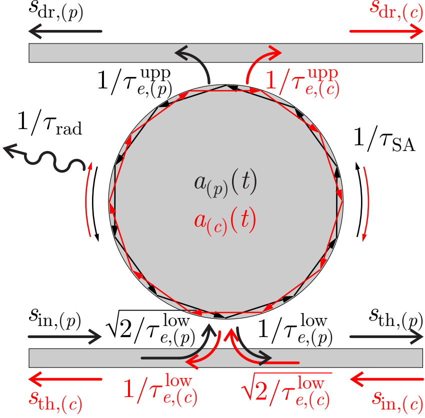
$s_{\mathrm{dr},(p)}$
$s_{\mathrm{dr},(c)}$
$1/\tau_{e,(p)}^{\mathrm{upp}}$
$1/\tau_{e,(c)}^{\mathrm{upp}}$
$1/\tau_{\mathrm{rad}}$
$1/\tau_{\mathrm{SA}}$
$a_{(p)}(t)$
$a_{(c)}(t)$
$s_{\mathrm{in},(p)}$
$\sqrt{2/\tau_{e,(p)}^{\mathrm{low}}}$
$1/\tau_{e,(p)}^{\mathrm{low}}$
$s_{\mathrm{th},(p)}$
$s_{\mathrm{th},(c)}$
$1/\tau_{e,(c)}^{\mathrm{low}}$
$\sqrt{2/\tau_{e,(c)}^{\mathrm{low}}}$
$s_{\mathrm{in},(c)}$

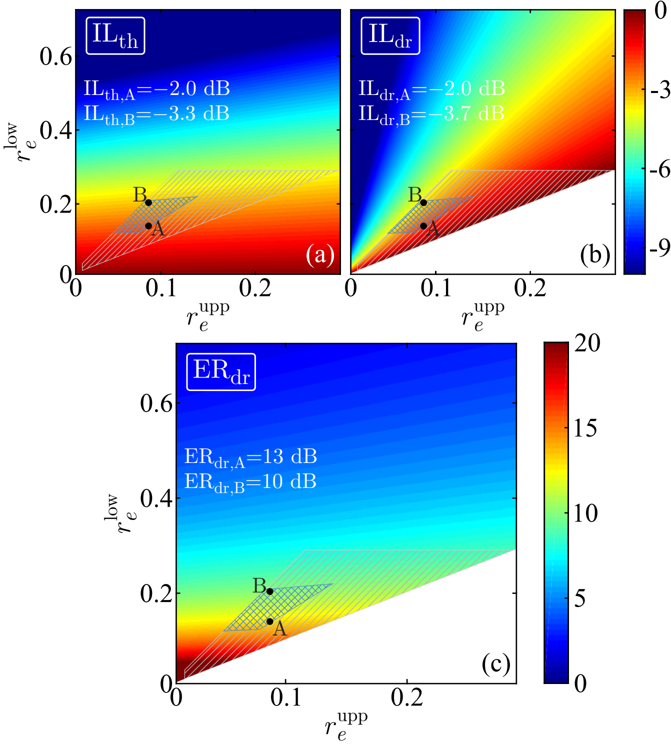
$\mathrm{IL_{th}}$
$\mathrm{IL_{th,A}}=-2.0$ dB
$\mathrm{IL_{th,B}}=-3.3$ dB
(a)
$\mathrm{IL_{dr}}$
$\mathrm{IL_{dr,A}}=-2.0$ dB
$\mathrm{IL_{dr,B}}=-3.7$ dB
(b)
0
-3
-6
-9
$\mathrm{ER_{dr}}$
$\mathrm{ER_{dr,A}}=13$ dB
$\mathrm{ER_{dr,B}}=10$ dB
(c)
20
15
10
5
0
A
B
r_e^{low}
r_e^{upp}
0
0.2
0.4
0.6
0.1

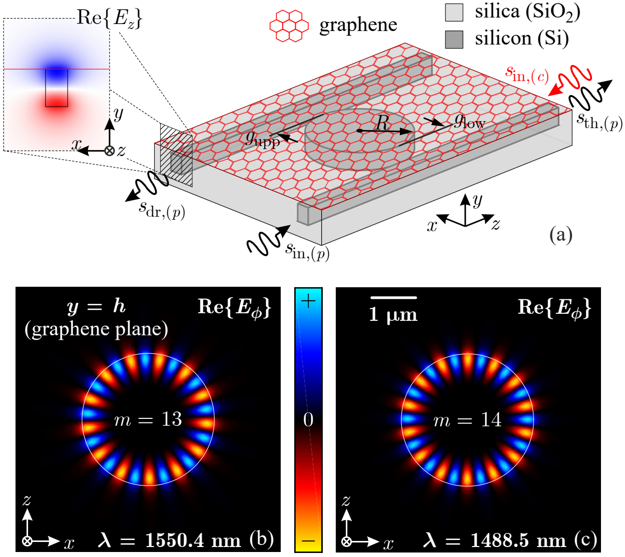
Re{E_z}
y
x
z
graphene
silica (SiO_2)
silicon (Si)
$s_{\mathrm{in},(c)}$
$s_{\mathrm{th},(p)}$
g_{upp}
R
g_{low}
$s_{\mathrm{dr},(p)}$
$s_{\mathrm{in},(p)}$
x y z
(a)
$y = h$
(graphene plane)
Re{E_ϕ}
$m = 13$
z x
λ = 1550.4 nm (b)
+
0
−
1 μm
Re{E_ϕ}
$m = 14$
z x
λ = 1488.5 nm (c)

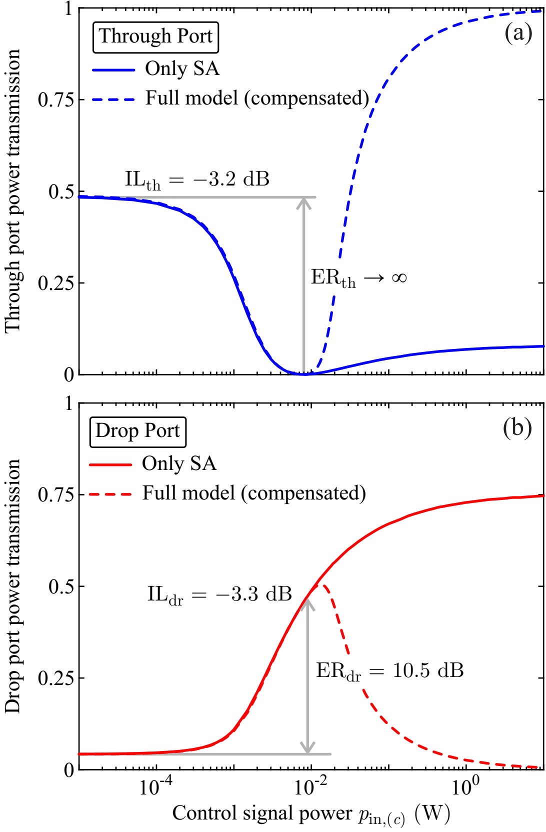
Through Port
(a)
Only SA
Full model (compensated)
$\mathrm{IL_{th}} = -3.2$ dB
$\mathrm{ER_{th}} \to \infty$
Through port power transmission
1
0.75
0.5
0.25
0
Drop Port
(b)
Only SA
Full model (compensated)
$\mathrm{IL_{dr}} = -3.3$ dB
$\mathrm{ER_{dr}} = 10.5$ dB
Drop port power transmission
1
0.75
0.5
0.25
0
10^{-4}
10^{-2}
10^{0}
Control signal power $p_{\mathrm{in},(c)}$ (W)

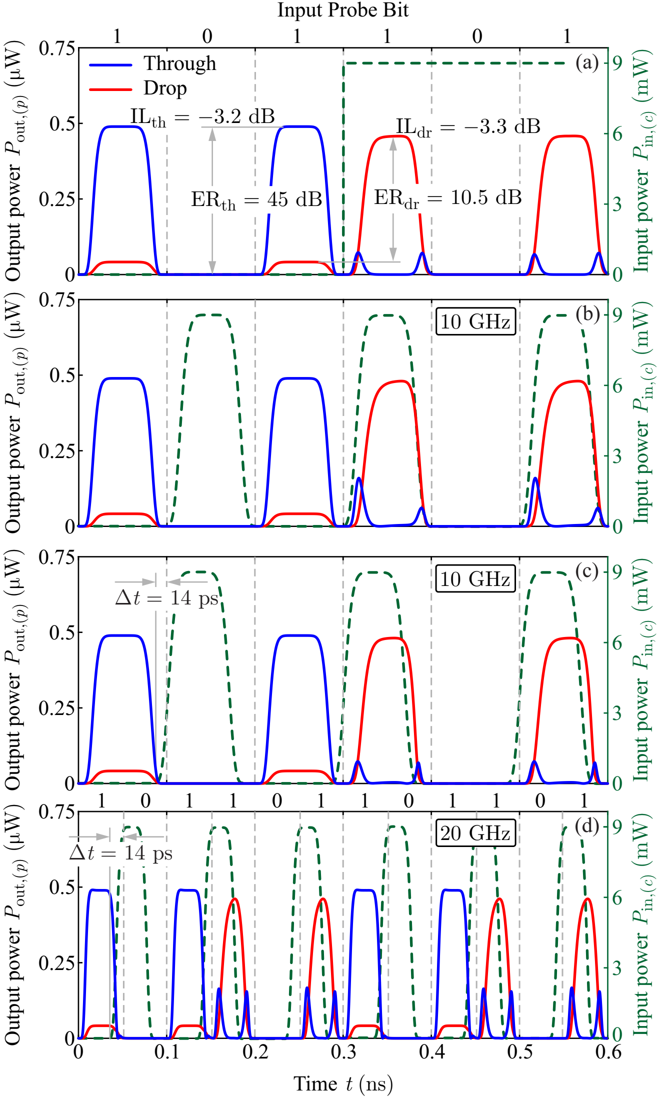
Input Probe Bit
1 0 1 1 0 1
Through
Drop
(a)
$\mathrm{IL_{th}} = -3.2$ dB
$\mathrm{ER_{th}} = 45$ dB
$\mathrm{IL_{dr}} = -3.3$ dB
$\mathrm{ER_{dr}} = 10.5$ dB
(b)
10 GHz
(c)
10 GHz
$\Delta t = 14$ ps
1 0 1 1 0 1 1 0 1 1 0 1
(d)
20 GHz
$\Delta t = 14$ ps
Output power $P_{\mathrm{out},(p)}$ (μW)
0 0.25 0.5 0.75
Input power $P_{\mathrm{in},(c)}$ (mW)
0 3 6 9
Time t (ns)
0 0.1 0.2 0.3 0.4 0.5 0.6